

Harnessing Multiple Folding Mechanisms in Soft Periodic Structures for Tunable Control of Elastic Waves

Sicong Shan, Sung H. Kang, Pai Wang, Cangyu Qu, Samuel Shian, Elizabeth R. Chen, and Katia Bertoldi*

Mechanical instabilities in periodic porous elastic structures may lead to the formation of homogeneous patterns, opening avenues for a wide range of applications that are related to the geometry of the system. This study focuses on an elastomeric porous structure comprising a triangular array of circular holes, and shows that by controlling the loading direction, multiple pattern transformations can be induced by buckling. Interestingly, these different pattern transformations can be exploited to design materials with highly tunable properties. In particular, these results indicate that they can be effectively used to tune the propagation of elastic waves in phononic crystals, enhancing the tunability of the dynamic response of the system. Using a combination of finite element simulations and experiments, a proof-of-concept of the novel material is demonstrated. Since the proposed mechanism is induced by elastic instability, it is reversible, repeatable, and scale-independent, opening avenues for the design of highly tunable materials and devices over a wide range of length scales.

1. Introduction

Porous materials with well-defined periodicity are ubiquitous not only in nature, but also in synthetic structures and devices.^[1] Periodic porous materials offer novel and unique properties, including light weight,^[2] high energy absorption,^[3] and the ability to control the propagation of both electromagnetic^[4] and elastic waves^[5,6] and heat flow.^[7] The properties and functionality of such materials are generally

determined by the deformation mechanisms of the ligaments, which buckle under compression at relatively low values of strain.

In elasto-plastic porous materials buckling of the beam-like ligaments results in collapse bands that progress at relatively constant stress, providing an efficient energy absorbing mechanism.^[8–12] However, this deformation process cannot be exploited to dynamically tune the macroscopic response of the system, since it is irreversible. By contrast, in periodic porous elastic structures, buckling of the ligaments may trigger dramatic homogeneous and reversible pattern transformations.^[13,14] Remarkably, it has been demonstrated that this parallel, cooperative buckling—a kind of “phase transition” from one to another microstructure—can be instrumental to design materials with tunable

properties, including systems with tunable negative Poisson's ratio,^[15] phononic^[16–18] and photonic^[19] switches and color displays.^[20]

Most of the porous systems studied so far are dual-shaped, since mechanical instability is found to trigger only one distinct new buckled pattern. Although different buckling modes have been observed in hexagonal honeycombs under biaxial compression depending on the loading conditions,^[1,9,10,21–23] the multiple pattern transformations induced by buckling have never been exploited to reversibly tune the properties of the system.

Here, we show that the ability to induce the formation of multiple ordered patterns in periodic porous elastic structures opens avenues for creating highly tunable systems. First, we develop a robust framework to identify periodic distributions of circular holes for which buckling and the direction of the applied loading can be exploited to form multiple folding patterns. Then, we confirm our findings through a combination of numerical simulations and experiments. Finally, we demonstrate numerically and experimentally that structures with multiple folding mechanisms open avenues for the design of highly tunable phononic crystals, whose response is effectively controlled by both the direction of loading and the magnitude of the applied deformation.

S. Shan, Dr. S. H. Kang, P. Wang, S. Shian,
Dr. E. R. Chen, Prof. K. Bertoldi
School of Engineering and Applied Sciences
Harvard University
Cambridge, Massachusetts 02138, USA
E-mail: bertoldi@seas.harvard.edu

C. Qu
School of Aerospace
Tsinghua University
Beijing 100084, China

Prof. K. Bertoldi
Kavli Institute
Harvard University
Cambridge, Massachusetts 02138, USA



DOI: 10.1002/adfm.201400665

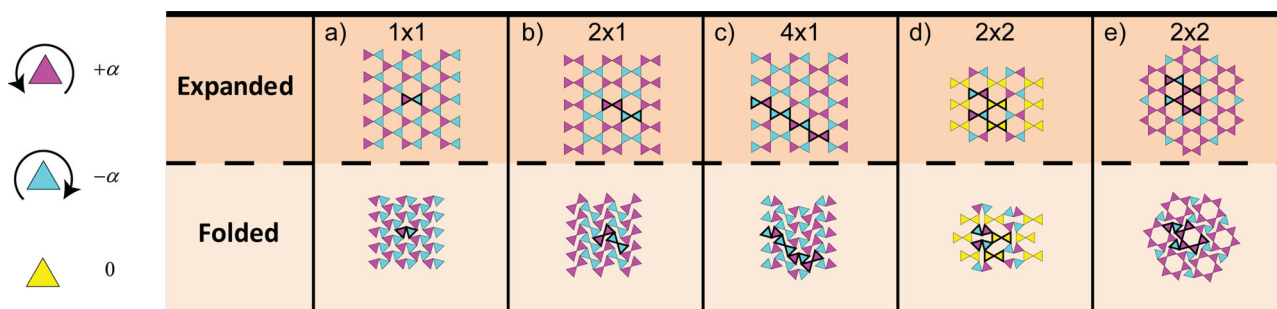


Figure 1. Schematic of the basic folding mechanisms in a rigid kagome network. The basic unit cell for each folding mechanism is outlined in black. The color of the triangles corresponds to their rotation. a) Mode with a basic cell of size 1×1 ; b) Mode with a basic cell of size 2×1 ; c) Mode with a basic cell of size 4×1 ; d) Mode with a basic cell of size 2×2 ; e) Mode with a basic cell of size 2×2 .

2. Design of Soft Periodic Structures with Multiple Folding Mechanisms

2.1. Periodic Networks of Rigid Polygons

To identify periodic porous elastic structures with multiple folding mechanisms, we start by investigating the flexibility of periodic planar networks built from rigid corner-connected polygons, which can rotate freely. While a network of connected squares has a single folding mechanism (see Supporting Information), it has been recently shown that in planar networks built from equilateral triangles the number of folding mechanisms grows with the size of unit cell.^[24] Here, we focus on the simplest of such tilings made of triangles – the kagome lattice. In this rigid network, the triangles are corner-connected to form hexagonal holes in the undeformed configuration and the smallest unit cell consists of only two triangles (see Figure 1-top).

If we consider a single unit cell (i.e. two corner-connected triangles) as a building block, it is easy to see that the periodic network has only one folding mechanism, in which all hexagonal holes progressively reduce to 3-point star-like shapes (see Figure 1a and Supporting Information). However, if we focus on a representative volume element (RVE) comprising an array of 1×2 unit cells (i.e. four corner-connected triangles) another folding mechanism emerges, resulting in a pattern of sheared voids where the shear direction alternates back and forth from row to row (see Figure 1b and Supporting Information). Finally, for a RVE consisting of 8 triangles, three other mechanisms are found: one consisting of alternating rows of sheared and 3-point star-like voids (see Figure 1c); another characterized by alternating rows of elongated holes oriented in horizontal and vertical direction and at $\pm 30^\circ$ with respect to the vertical direction (see Figure 1d); and a chiral pattern comprising six highly deformed voids surrounding an undeformed one (see Figure 1e).

Additional folding mechanisms can then be identified by considering larger RVEs (see Supporting Information). However, all these mechanisms share the same basic elements found in the patterns shown in Figure 1. We also note that in all the identified folding mechanisms the triangles are found either to rotate by $\pm\alpha$ (i.e. by the same amount either in clockwise or anti-clockwise direction, see magenta and cyan triangles in Figure 1) or not to rotate at all (i.e. $\alpha = 0$, see yellow triangles in Figure 1), facilitating the construction of folding mechanisms for large RVEs.

Finally, given the finite size of the elastomeric samples considered in this study, it is worth pointing out that we expect only the basic folding mechanisms shown in Figure 1 to be triggered during loading.

2.2. From Networks of Rigid Polygons to Continuum Porous Structures

Having found a planar network built from rigid corner connected triangles with multiple folding mechanisms, we then identify the corresponding porous structure. This can be easily done by replacing all the hexagonal voids with circular ones,^[25] as shown in Figure 2. It is interesting to see that the outcome of this simple process is a porous structure comprising a periodic array of circular holes on a triangular lattice. In this continuum structure all the hinges of the original kagome network are replaced by thin ligaments and we expect these ligaments to buckle during loading.

Although the stability under biaxial compression of similar structures such as hexagonal honeycombs has been previously studied,^[1,9,10,21–23] the ability to induce multiple pattern transformations has never been exploited to design materials and devices with enhanced tunability. In the next sections we investigate both numerically and experimentally how loading paths

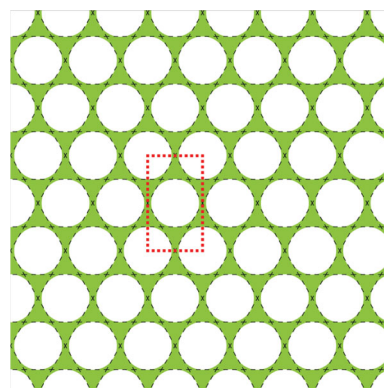


Figure 2. From a rigid networks of triangles to its corresponding continuum structure. All the hinges of the original kagome network (dashed black line) are replaced by thin ligaments in the continuum structure (shaded in green). The dotted red line indicates the unit cell of the structure.

with different angles can be exploited to trigger the different folding mechanisms shown in Figure 1, enabling the design of materials with highly tunable responses.

3. Mechanics of Soft Periodic Structures with Multiple Folding Mechanisms

3.1. Numerical Analysis

We continue by performing finite element (FE) simulations to investigate the patterns induced by buckling in a triangular array of circular holes in an elastomeric matrix. We focus on a structure characterized by an initial porosity $\Psi_0 = 70\%$ and assume plane strain conditions. The nonlinear finite-element code ABAQUS/STANDARD is used to deform the structures as well as to investigate its stability. For all the analyses, 2D finite element models are constructed using triangular quadratic elements (element type CPE6H in ABAQUS) and the accuracy of the mesh is ascertained through a mesh refinement study. Moreover, the response of the silicone rubber used in the experiments to cast the samples is captured using the incompressible Neo-Hookean hyperelastic model^[26] with initial shear modulus μ_0 .

Since the finite-sized specimens are necessarily influenced by boundary conditions at the edges, we focus on the response of the corresponding infinite periodic structure and study the response of rectangular RVEs by applying periodic boundary conditions.^[27,28] We investigate the response of the porous structure under biaxial loading so that the macroscopic deformation gradient \mathbf{F} is given by

$$\mathbf{F} = (1 + \varepsilon_{xx})\mathbf{e}_x \otimes \mathbf{e}_x + (1 + \varepsilon_{yy})\mathbf{e}_y \otimes \mathbf{e}_y + \mathbf{e}_z \otimes \mathbf{e}_z, \quad (1)$$

where ε_{xx} and ε_{yy} denote the macroscopically applied nominal strains and \mathbf{e}_x , \mathbf{e}_y and \mathbf{e}_z are the basis vectors of Cartesian coordinates.

Without loss of generality, we focus our attention to proportional straining paths in principal nominal strain space. More specifically, we assume that the ratio of the principal nominal strains is fixed, namely:

$$\varepsilon_{xx} = \lambda \cos(\theta), \varepsilon_{yy} = \lambda \sin(\theta) \quad (2)$$

where λ is the monotonically increasing load parameter and θ is the load path angle. In this study we consider $\pi \leq \theta \leq 3\pi/2$ to investigate various biaxial compression loading conditions. To facilitate the comparison between deformed configurations obtained for different values of θ , we also introduce the areal strain defined as^[29]

$$\begin{aligned} \varepsilon_{Area} &= \frac{A - A_0}{A_0} = (1 + \varepsilon_{xx})(1 + \varepsilon_{yy}) - 1 \\ &= \lambda(\cos(\theta) + \sin(\theta)) + \lambda^2 \cos(\theta)\sin(\theta) \end{aligned} \quad (3)$$

A_0 and A denote the area of the RVE in the undeformed and deformed configuration, respectively.

To understand the patterns emerging as the result of buckling in the structure, we start by investigating the stability of

the system. Taking the rectangular domain highlighted by red box in Figure 2 as unit cell, we consider RVEs consisting of $m \times n$ cells subjected to periodic boundary conditions. For a given value of θ we progressively load each RVE and calculate its natural frequency along the loading path, accounting for the effect of large deformation induced by loading. As an example, in Figure 3a we show the results of the stability analysis for an RVE comprising 2×2 unit cells and loading path angle $\theta = \pi$. In the undeformed configuration (i.e. $\lambda = 0$) all eigenvalues ω^2 are positive. However, as λ increases, the eigenvalues associated with each mode gradually decrease and eventually become negative. The critical loading parameter λ_{cr} associated with each mode can be easily extracted from the data, since it corresponds to the intersection point between each curve and the horizontal line $\omega^2 = 0$.

For this specific case, we find that the lowest critical loading parameter $\lambda_{cr,1} = 0.0331$ is associated with a mode that resembles the folding mechanism shown in Figure 1d for the kagome network. Here and in the following we refer to this mode as to the X-mode. The second mode is then triggered at $\lambda_{cr,2} = 0.0357$, resulting in a pattern similar to that reported in Figure 1b, which we denote as Z-mode. Subsequently, the third and fourth modes are found at $\lambda_{cr,3} = \lambda_{cr,4} = 0.0476$ consisting of alternating rows of sheared and 3-point star-like voids as that shown in Figure 1c. Finally the fifth mode is triggered at $\lambda_{cr,5} = 0.0665$, comprising an array of 3-point star-like voids as that reported in Figure 1a.

Identical calculations are then repeated for RVEs of different sizes and the critical strain of the infinite periodic structure for the given load path angle θ is then defined as the minimum of λ_{cr} on all possible periodic RVEs. In Figure 3b we report the critical strains for periodic RVEs with $m \times n$ cells for $\theta = \pi$. The results indicate that the critical loading parameter is the minimum for RVEs comprising an even number of unit cells in both directions and it is associated with the X-mode. Higher λ_{cr} is found for RVEs with an odd number of unit cells either in vertical or horizontal direction, for which the Z-mode is found to be critical. Therefore, when the structure is compressed with loading path angle $\theta = \pi$, we expect the X-mode to be triggered during loading.

Finally, to construct the instability surface we repeat the same calculations for different loading path angles θ . We first note that for all considered values of θ , the X- and Z-mode are always triggered either as first or second mode. In Figure 3c we then plot the critical load parameter associated with the X- and Z-mode as a function of θ . The critical load parameter λ_{cr} associated with the X-mode is found to decrease at first, to reach a minimum at $\theta = (5/4 - 1/36)\pi$ and then to progressively increase. Similar behavior is found for the critical loading parameter associated to the Z-mode, but in this case the minimum occurs at $\theta = (5/4 + 1/36)\pi$. Interestingly, for $\theta < 5\pi/4$ the critical loading parameter λ_{cr} associated to the X-mode is always lower than that corresponding to the Z-mode, so that the X-mode is expected to emerge during deformation for this range of loading path angles. By contrast, the Z-mode is expected to be triggered when $5\pi/4 < \theta < 3\pi/2$, since in this case the lowest critical loading parameter is that corresponding to the Z-mode. Finally, it is worth noting that both the X- and Z-mode are characterized by the same critical loading parameter for $\theta = 5\pi/4$, suggesting that for this specific loading

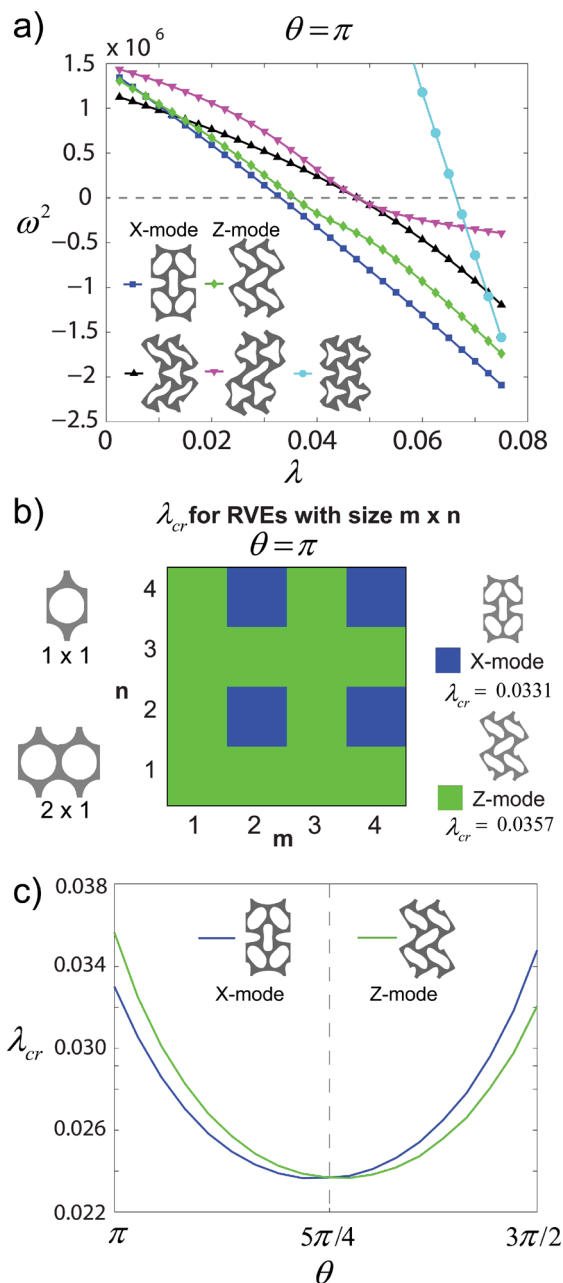


Figure 3. Numerical study of the instability of a periodic structure with multiple folding mechanisms. a) Evolution of eigenvalues at different levels of compression (loading along $\theta = \pi$ path) and corresponding deformation modes. The intersection points of each curve with the horizontal line $\omega^2 = 0$ corresponds to the critical loading parameter λ_{cr} for each mode. b) Critical loading parameter λ_{cr} for RVEs consisting of $m \times n$ unit cells (loading along $\theta = \pi$ path), where a unit cell consists of a rectangular domain with two voids. The results indicate that configurations with even number of unit cells along the two directions have the minimum critical strain. c) Critical loading parameter λ_{cr} associated to the X-mode (blue line) and Z-mode (green line) as a function of the loading path angle θ .

direction a pattern corresponding to a linear combination of both modes may be triggered.

Next, guided by the stability analysis we conduct a post buckling analysis on a RVE consisting of 2×2 unit cells by applying

periodic boundary conditions and introducing a geometrical imperfection with the form of the first two eigenmodes. In Figure 4a, c and e we report numerical predictions of the pattern evolution for $\theta = \pi$, $5\pi/4$ and $3\pi/2$ at different values of areal strain ϵ_{Area} . Initially, the circular holes deform gradually and homogeneously. However, a transformation to a strikingly different pattern is triggered very early along the loading path (see images at $\epsilon_{Area} = -0.05$) and the new patterns become further accentuated in shape with increasing strain as seen in the images at $\epsilon_{Area} = -0.10$, -0.15 , -0.20 and -0.25 . As predicted by the stability analysis, the structure deforms into the X- and Z-mode when $\theta = \pi$ and $3\pi/2$, respectively.

However, a new chiral pattern resembling that reported in Figure 1e for the kagome network emerges when the structure is compressed equibiaxially (i.e. $\theta = 5\pi/4$). Interestingly, this chiral pattern does not correspond to one of the modes predicted by the stability analysis, but it can be obtained as a linear combination of the X- and Z-mode (see Supporting Information).

3.2. Experiments

To verify our numerical analysis, we fabricate centimeter scale elastomeric structures comprising 10×12 unit cells and characterized by initial porosity $\Psi_0 = 70\%$, hole diameter $D_0 = 8$ mm and out-of-plane thickness ~ 50 μm . The samples for the experiments are fabricated using silicone rubber (Mold Max 60 from Smooth-On Inc, Young's modulus $E = 2.16$ MPa) and a mold-casting process with molds prepared by 3D rapid prototyping. In-plane biaxial compression tests are performed using a custom-built testing set-up with four linear stages (see Supporting Information).

Representative pictures taken during the tests at different levels of ϵ_{Area} are presented in Figure 4b, d and f for $\theta = \pi$, $5\pi/4$ and $3\pi/2$, respectively. We start by noting that there is excellent agreement between numerical (Figure 4a, c and e) and experimental (Figure 4b, d and f) results. In particular, the effect of the boundary conditions is found to be negligible and the pattern transformations induced by instability are remarkably uniform across the samples, so that the behavior of the finite size sample does not deviate from that of the infinite periodic structure investigated numerically. Note that for the tests performed with $\theta = \pi$ and $\theta = 3\pi/2$, we do not constrain the deformation in lateral direction, since we find the lateral strain to be negligible (more specifically, we find the absolute value of lateral strain to be less than 0.05). Finally, since the specimens are made of an elastomeric material, the process is fully reversible and repeatable. Upon release of the applied loading condition, the deformed samples recover their original configurations, suggesting that this deformation mechanism can be exploited for the design of materials with tunable properties.

4. Harnessing Multiple Folding Mechanisms to Design Tunable Phononic Crystals

Having demonstrated that multiple folding mechanism can be easily triggered in a triangular array of circular voids by simply changing the loading path angle θ , in this section we show that the

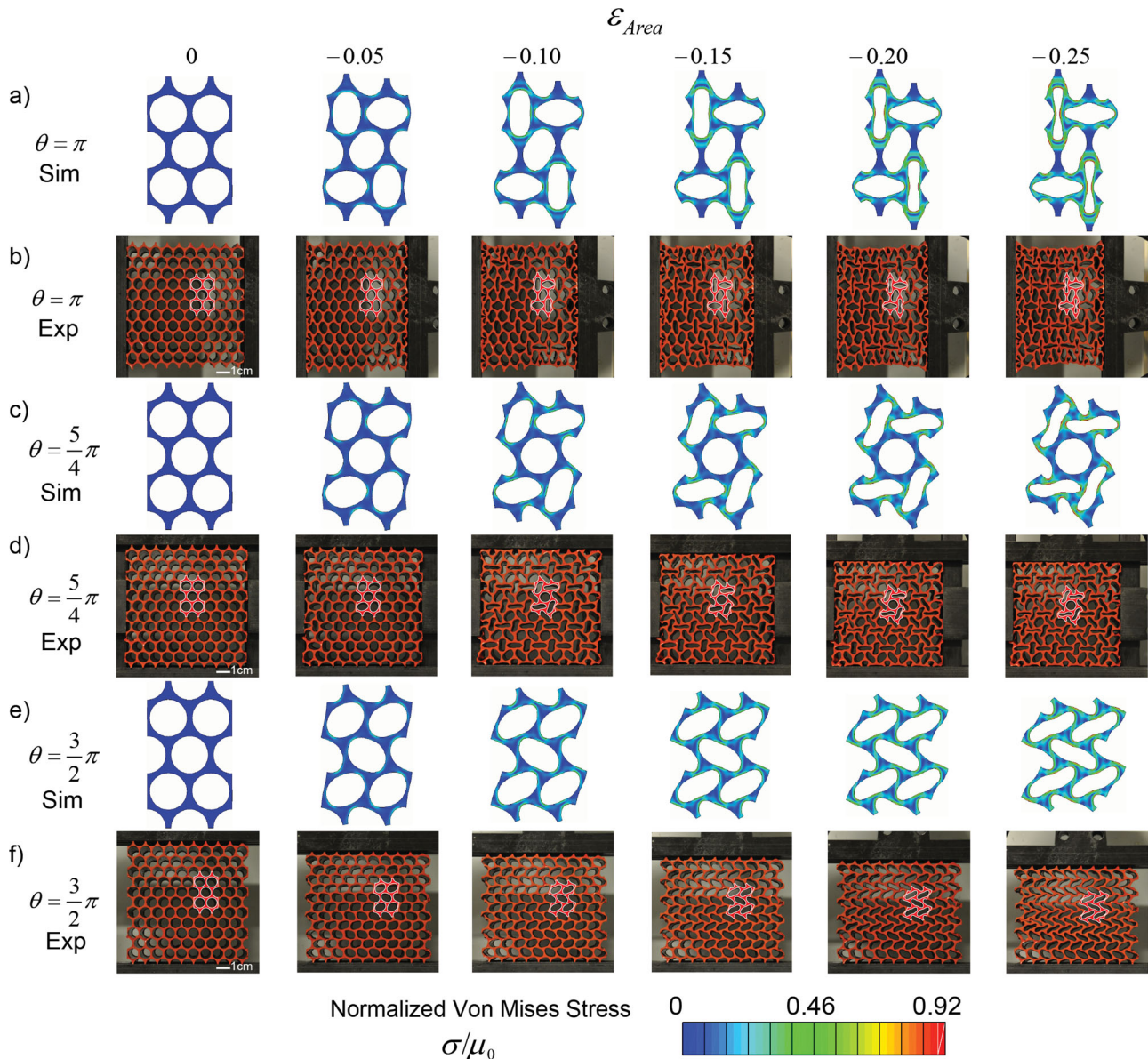


Figure 4. Numerical and experimental images of the triangular lattice loaded along $\theta = \pi$ (a and b), $\theta = 5\pi/4$ (c and d), $\theta = 3\pi/2$ (e and f) at different levels of deformation. The results show three distinct folding mechanisms: X-mode under horizontal compression (i.e. $\theta = \pi$), Z-mode under vertical compression (i.e. $\theta = 3\pi/2$) and a chiral mode under equibiaxial compression (i.e. $\theta = 5\pi/4$). The deformed shapes from simulation (colored in bright-red and outlined in white) are superimposed on the experimental pictures showing excellent agreement. For the numerical images, we also show the normalized Von Mises stress distributions in the deformed configurations.

system can be exploited to design highly tunable phononic crystals for the control and manipulation of elastic wave propagation.

Phononic crystals are periodic structures in which Bragg scattering is exploited to effectively filter elastic waves by the generation of bandgaps—frequency ranges of strong wave attenuation—at wavelengths comparable to the unit cell size.^[5] Motivated by technological applications such as the design of waveguides,^[30–36] frequency modulators,^[31] noise reduction devices,^[37–39] and vibration isolators,^[40,41] the effects of both material properties,^[42–44] and geometry (i.e., volume fraction and topology)^[45,46] on the characteristics of phononic crystals have been investigated. Moreover, it has been recently

recognized that large deformations induced by instabilities can be exploited to design phononic crystals whose bandgap position and width can be reversibly tuned.^[16–18] Here, we show both numerically and experimentally that the tunability of the periodic system can be greatly enhanced in the presence of multiple folding mechanisms.

4.1. Numerical Analysis

To investigate the effect of different instability-induced patterns on the propagation of small amplitude elastic waves in

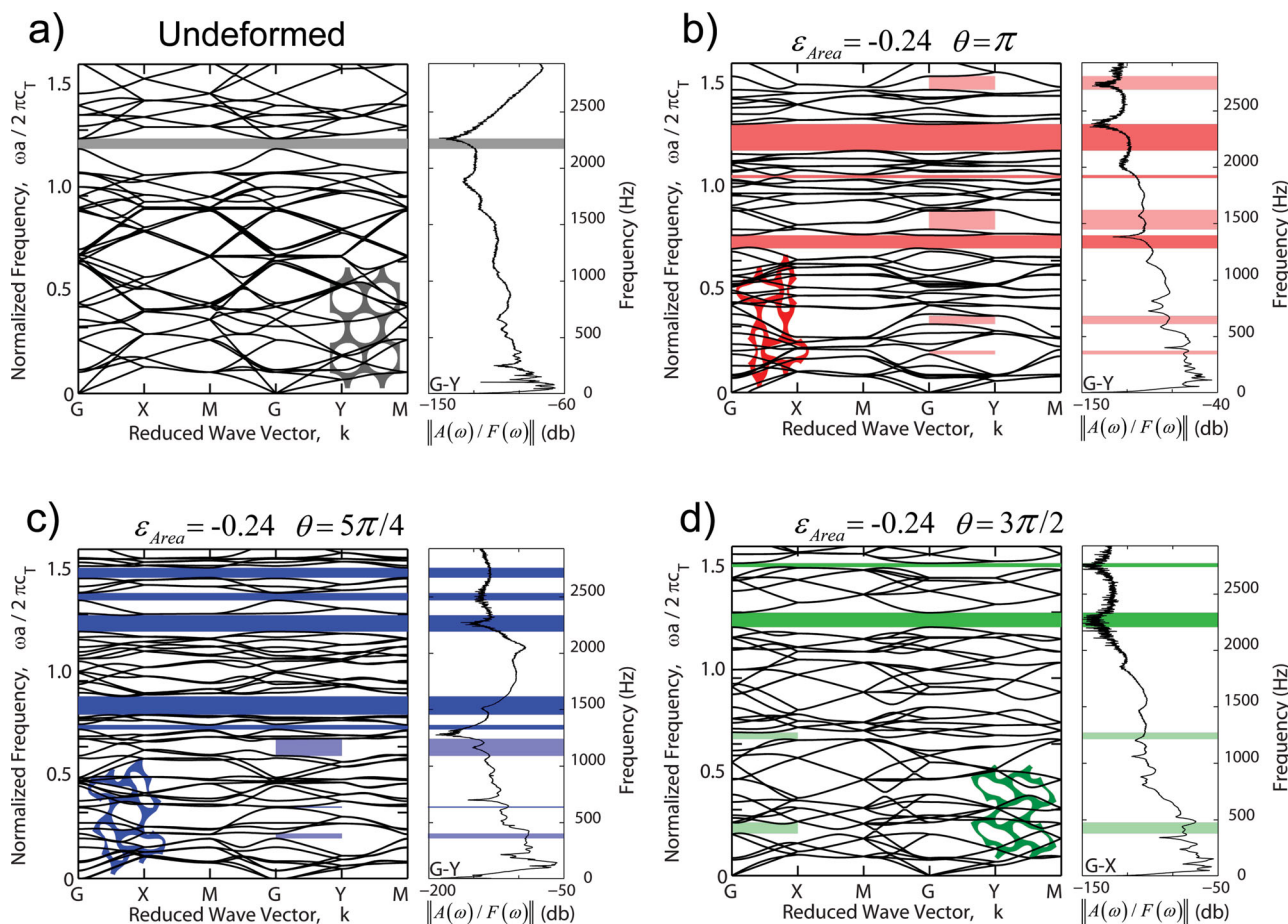


Figure 5. Comparison between the numerical dispersion relations (left) and the experimental frequency response functions (right) of the system obtained for different values of θ .

the periodic structure, we first conduct finite element analysis (see Supporting Information). We start by constructing the dispersion diagram for the undeformed configuration, as shown in **Figure 5a**. When undeformed, the periodic structure possesses a complete band gap (i.e. bandgap for all directions of wave propagation) for $\tilde{f} = \omega a / (2\pi c_T) = 1.189 - 1.238$, where ω is the angular frequency of the propagating wave, the lattice constant $a = 10$ mm is defined as the center-to-center distance between holes in the undeformed configuration and $c_T = 18.3$ m/s is the transverse speed of sound in the constituting homogeneous elastomeric material. Therefore, elastic waves with $f = \omega / (2\pi)$ in the range 2176–2266 Hz are not allowed to propagate within the undeformed structure due to the bandgap.

Next, we investigate the effect of the applied load on the propagation of elastic waves, by considering three deformed configurations obtained by different loading path angles $\theta = \pi$, $5\pi/4$ and $3\pi/2$, but under the same areal strain, $\epsilon_{Area} = -0.24$. As shown in **Figure 4**, these three different values of q result in three distinct patterns. Interestingly, the dispersion diagrams shown in **Figure 5-b, -c** and **-d** indicate that the variation in patterns has a strong effect on the propagation of elastic waves, demonstrating that in periodic elastic structures with multiple folding mechanisms the band gaps can be dramatically altered

not only by the extent of deformation but also by the choice of the loading path.

In fact, when the X-mode is triggered (i.e. $\theta = \pi$), the pre-existing complete band gap is shifted and widened to $\tilde{f} = 1.180 - 1.307$. In addition, two new complete band gaps that do not exist in the undeformed structure appear at $\tilde{f} = 0.699 - 0.765$ and $\tilde{f} = 1.045 - 1.070$. Differently, for $\theta = 5\pi/4$ the chiral folding mechanism is triggered and in this case the system is characterized by five complete band gaps for $\tilde{f} = 0.724 - 0.745$, $0.795 - 0.884$, $1.199 - 1.278$, $1.351 - 1.386$, and $1.461 - 1.509$. Finally, the Z-mode is triggered for $\theta = 3\pi/2$ and in this case the deformation is found to widen the pre-existing complete band gap and to open only one complete new band gap for $\tilde{f} = 1.207 - 1.277$.

4.2. Experiments

To validate the predictions of the numerical simulations, frequency response measurements of the elastomeric structure are made using an electro-dynamic shaker directly connected to one end of samples through a load cell to provide vibrations.

The dynamic response is recorded using a miniature accelerometer attached to the far end of the sample (see Supporting

Information). Measurements are conducted at different level of deformation and the transmittance is computed as the ratio between the output acceleration signal recorded at the far end of the sample and the input force signal from the load cell (i.e., $||A(\omega)/F(\omega)||$).

Figure 5 shows the comparison between numerical and experimental results. For each of the four panels in Figure 5, the dispersion plots on the left are calculated numerically and plots on the right show the transmittance curves from experiments. Here, the numerical calculations consider all propagation directions in an infinitely periodic structure, while the experimental results are shown for only one propagation direction (G-Y direction for Figure 5a, b and c; G-X direction for d). Nevertheless, we still observe a good match between these two sets of results. In the undeformed case, the experimental response indicates an apparent attenuation at the numerically calculated band gap frequency. After the structure is deformed into different patterns, the calculated complete band gaps can still find their signatures in the experimental results, with very few exceptions due to finite-size boundary effects that are not investigated in this study. Furthermore, the transmittance curves from experiments also exhibit some features of directional band gaps, indicated by the lighter color-shaded areas in Figure 5.

5. Conclusion

We demonstrated both numerically and experimentally the design of highly tunable phononic crystals by harnessing multiple folding mechanisms in periodic elastomeric structures comprising a triangular array of circular holes. We started with a geometrical analysis of 2D rigid periodic networks and found that a kagome lattice can have multiple folding mechanisms.

Guided by these results, we rationally designed the corresponding continuum soft periodic porous structure and showed that three different patterns induced by buckling can be triggered during compressive loading by changing the direction of loading. Remarkably, the dynamic response of the system was found to be highly affected by the pattern induced by buckling, demonstrating that the band gaps can be tuned both by deformation mode and the extent of deformation.

Our finding opens new opportunities to design multifunctional devices with enhanced tunability because (i) the mechanism can be applied to various length-scales; (ii) the various patterns can be triggered upon application of different stimuli and using different materials; (iii) the process is fully reversible and (iv) more importantly, the formation of different patterns can be easily controlled by changing the loading direction. By engineering geometry, length scales, and materials, we can envision smart systems that control the wave propagation autonomously depending on the loading conditions.

6. Experimental Section

Please see the Supporting Information for experimental details.

Supporting Information

Supporting Information is available from the Wiley Online Library or from the author.

Acknowledgements

This work has been supported by NSF through grant DMR-0820484 (Harvard MRSEC) and grant CMMI-1149456 (CAREER) and by the Wyss Institute through the Seed Grant Program. K.B. acknowledges start-up funds from the Harvard School of Engineering and Applied Sciences and the support of the Kavli Institute at Harvard University. E.R.C. acknowledges NSF MSPRF grant DMS-1204686. The authors wish to thank Prof. David Clarke for the help with the experiments and Dr. Fillippo Casadei for useful discussions.

Received: February 26, 2014

Published online:

- [1] L. Gibson, M. Ashby, *Cellular Solids: Structure and Properties*, Cambridge University Press, Cambridge **1999**.
- [2] T. Schaedler, A. Jacobsen, A. Torrents, A. Sorensen, J. Lian, J. Greer, L. Valdevit, W. Carter, *Science* **2011**, *334*, 962–965.
- [3] J.-H. Lee, L. Wang, M. C. Boyce, E. L. Thomas, *Nano Lett.* **2012**, *12*, 4392–4396.
- [4] D. Schurig, J. J. Mock, B. J. Justice, S. A. Cummer, J. B. Pendry, A. F. Starr, D. R. Smith, *Science* **2006**, *314*, 977–980.
- [5] M. S. Kushwaha, P. Halevi, L. Dobrzynski, B. Djafari-Rouhani, *Phys. Rev. Lett.* **1993**, *71*, 2022–2025.
- [6] M. Maldovan, E. L. Thomas, *Periodic Materials and Interference Lithography for Photonics, Phononics and Mechanics*, Wiley-VCH, Weinheim **2009**.
- [7] M. Maldovan, *Phys. Rev. Lett.* **2013**, *110*, 025902.
- [8] T. Wierzbicki, W. Abramowicz, *J. Appl. Mech.* **1983**, *50*, 727–734.
- [9] S. Papka, S. Kyriakides, *Int. J. Solids Struct.* **1999**, *36*, 4367–4396.
- [10] S. Papka, S. Kyriakides, *Int. J. Solids Struct.* **1999**, *36*, 4397–4423.
- [11] E. Wu, W. Jiang, *Int. J. Impact Eng.* **1997**, *19*, 439–456.
- [12] A. M. Hayes, A. Wang, B. M. Dempsey, D. L. McDowell, *Mech. Mater.* **2004**, *36*, 691–713.
- [13] T. Mullin, S. Deschanel, K. Bertoldi, M. C. Boyce, *Phys. Rev. Lett.* **2007**, *99*, 084301.
- [14] Y. Zhang, E. A. Matsumoto, A. Peter, P. Lin, R. D. Kamien, S. Yang, *Nano Lett.* **2008**, *8*, 1192–1196.
- [15] K. Bertoldi, P. Reis, S. Willshaw, T. Mullin, *Adv. Mater.* **2010**, *22*, 361–366.
- [16] K. Bertoldi, M. C. Boyce, *Phys. Rev. B* **2008**, *77*, 052105.
- [17] J. Jang, C. Y. Koh, K. Bertoldi, M. C. Boyce, E. L. Thomas, *Nano Lett.* **2009**, *9*, 2113–2119.
- [18] P. Wang, J. Shim, K. Bertoldi, *Phys. Rev. B* **2013**, *88*, 014304.
- [19] D. Krishnan, H. Johnson, *J. Mech. Phys. Solids* **2009**, *57*, 1500–1513.
- [20] J. Li, J. Shim, J. Deng, J. T. B. Overvelde, X. Zhu, K. Bertoldi, S. Yang, *Soft Matter* **2012**, *8*, 10322–10328.
- [21] L. Gibson, M. Ashby, J. Zhang, T. Triantafillou, *Int. J. Solids Struct.* **1989**, *31*, 635–663.
- [22] J. Chung, A. Waas, *J. Eng. Mech.* **2001**, *127*, 180–193.
- [23] N. Ohno, D. Okumura, H. Noguchi, *J. Mech. Phys. Solids* **2002**, *50*, 1125–1153.
- [24] V. Kapko, M. Treacy, M. Thorpe, S. Guest, *Proc. R. Soc. A* **2009**, *465*, 3517–3530.
- [25] J. Shim, S. Shan, A. Kosmrlj, S. H. Kang, E. R. Chen, J. C. Weaver, K. Bertoldi, *Soft Matter* **2013**, *9*, 8198–8202.
- [26] R. W. Ogden, *Nonlinear Elastic Deformations*, Dover, New York **1998**.

- [27] M. Danielsson, D. Parks, M. Boyce, *J. Mech. Phys. Solids* **2002**, *50*, 351–379.
- [28] K. Bertoldi, M. C. Boyce, S. Deschanel, S. M. Prange, T. Mullin, *J. Mech. Phys. Solids* **2008**, *56*, 2642–2668.
- [29] D. Needham, R. Nunn, *Biophys. J.* **1990**, *58*, 997–1009.
- [30] A. Khelif, A. Choujaa, S. Benchabane, B. Djafari-Rouhani, V. Laude, *Appl. Phys. Lett.* **2004**, *84*, 4400–4402.
- [31] M. Kafesaki, M. M. Sigalas, N. Garcia, *Phys. Rev. Lett.* **2000**, *85*, 4044–4047.
- [32] A. Khelif, B. Djafari-Rouhani, J. O. Vasseur, P. A. Deymier, P. Lambin, L. Dobrzynski, *Phys. Rev. B* **2002**, *65*, 174308.
- [33] J.-H. Sun, T.-T. Wu, *Phys. Rev. B* **2005**, *71*, 174303.
- [34] J.-H. Sun, T.-T. Wu, *IEEE Ultrasonics Symposium* **2006**, *1*, 673.
- [35] J.-H. Sun, T.-T. Wu, *Phys. Rev. B* **2007**, *76*, 104304.
- [36] J. O. Vasseur, A. Hennion, B. Rouhani, F. Duval, B. Dubus, Y. Pennec, *J. App. Phys.* **2007**, *101*, 114904.
- [37] D. Elser, U. L. Andersen, A. Korn, O. Glöckl, S. Lorenz, C. Marquardt, G. Leuchs, *Phys. Rev. Lett.* **2006**, *97*, 133901.
- [38] T. Elnady, A. Elsabbagh, W. Akl, O. Mohamady, V. M. Garcia-Chocano, D. Torrent, F. Cervera, J. Sanchez-Dehesa, *Appl. Phys. Lett.* **2009**, *94*, 134104.
- [39] F. Casadei, L. Dozio, M. Ruzzene, K. Cunefare, *J. Sound. Vib.* **2010**, *329*, 3632.
- [40] Y. Dian-Long, L. Yao-Zong, Q. Jing, Z. Hong-Gang, L. Zhi-Ming, *Chin. Phys. Lett.* **2005**, *22*, 1958.
- [41] F. Casadei, B. Beck, K. A. Cunefare, M. Ruzzene, *Int. J. Solids Struct.* **2012**, *23*, 1169.
- [42] D. Bria, B. Djafari-Rouhani, *Phys. Rev. E* **2002**, *66*, 056609.
- [43] J. O. Vasseur, B. Djafari-Rouhani, L. Dobrzynski, M. S. Kushwaha, P. Halevi, *J. Phys. Condensed Mat.* **1994**, *6*, 8759.
- [44] X.-Z. Zhou, Y.-S. Wang, C. Zhang, *J. App. Phys.* **2009**, *106*, 014903.
- [45] J.-B. Li, Y.-S. Wang, C. Zhang, *J. Vib. Acoust.* **2013**, *135*, 031015.
- [46] A. Movchan, N. Movchan, S. Haq, *Mat. Sci. Eng.* **2006**, *431*, 175183.

ADVANCED FUNCTIONAL MATERIALS

Supporting Information

for *Adv. Funct. Mater.*, DOI: 10.1002/adfm.201400665

Harnessing Multiple Folding Mechanisms in Soft Periodic Structures for Tunable Control of Elastic Waves

*Sicong Shan, Sung H. Kang, Pai Wang, Cangyu Qu, Samuel Shian, Elizabeth R. Chen, and Katia Bertoldi**

Supporting Information for *Harnessing multiple folding mechanisms in soft periodic structures for tunable control of elastic waves*

Sicong Shan,¹ Sung H. Kang,¹ Pai Wang,¹ Cangyu Qu,² Samuel Shian,¹ Elizabeth R. Chen,¹ and Katia Bertoldi^{1,3}

¹*School of Engineering and Applied Sciences, Harvard University, Cambridge, Massachusetts 02138, USA*

²*School of Aerospace, Tsinghua University, Beijing, China, 100084*

³*Kavli Institute, Harvard University, Cambridge, Massachusetts 02138, USA*

PERIODIC NETWORKS OF RIGID POLYGONS

To identify periodic porous elastic structures with multiple folding mechanisms, we investigate the flexibility of periodic planar networks built from rigid corner-connected (hinged) polygons, which can rotate freely around the hinges. First, we show that a network of connected squares has a single folding mechanism. Then, as previously demonstrated by Guest *et al.* [1], we show that in planar networks built from equilateral triangles the number of folding mechanisms grows with the size of unit cell.

Network of rigid squares

We start by investigating the folding mechanisms of a network of connected squares. To demonstrate that this structure has a single folding mechanism, we consider unit cells of different sizes and determine their folding mechanisms by enforcing geometric compatibility. We first focus on a unit cell consisting of two connected squares and show that in this case no folding mechanism is supported by the network. Then, we consider a unit cell comprising four squares and show that in this case only one folding mechanism exists. Our simple analysis can be extended to larger unit cells, indicating that only one single folding mechanism is possible for this network (for the sake of brevity here we do not report results for unit cells with more than four squares).

Unit cell with two squares

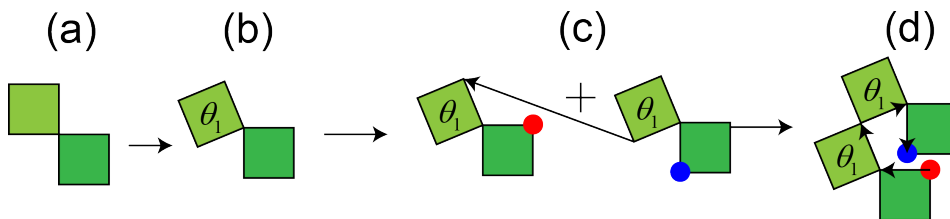


Figure S1: Geometrical compatibility of a unit cell with two squares. θ_1 indicates the rotation angle of the light-green square. Geometrical compatibility between adjacent unit cells requires the red and blue markers overlap.

Here we consider a unit cell consisting of two corner-connected squares with edge L_0 (see Fig. S1-a). If one of the two squares rotate by an angle θ_1 , geometrical compatibility requires that the red and blue circular markers in Fig. S1-c overlap, yielding

$$L_0 \cos(\pi) + L_0 \cos\left(\frac{\pi}{2} + \theta_1\right) + L_0 \cos(0 + \theta_1) + L_0 \cos\left(-\frac{\pi}{2}\right) = 0, \quad (\text{S1})$$

$$L_0 \sin(\pi) + L_0 \sin\left(\frac{\pi}{2} + \theta_1\right) + L_0 \sin(0 + \theta_1) + L_0 \sin\left(-\frac{\pi}{2}\right) = 0.$$

It is easy to show that Eqs. (S1) are both satisfied only when $\theta_1 = 0$, indicating that no folding mechanism is supported by the network when a unit cell consisting of two squares is considered.

Unit cell with four squares

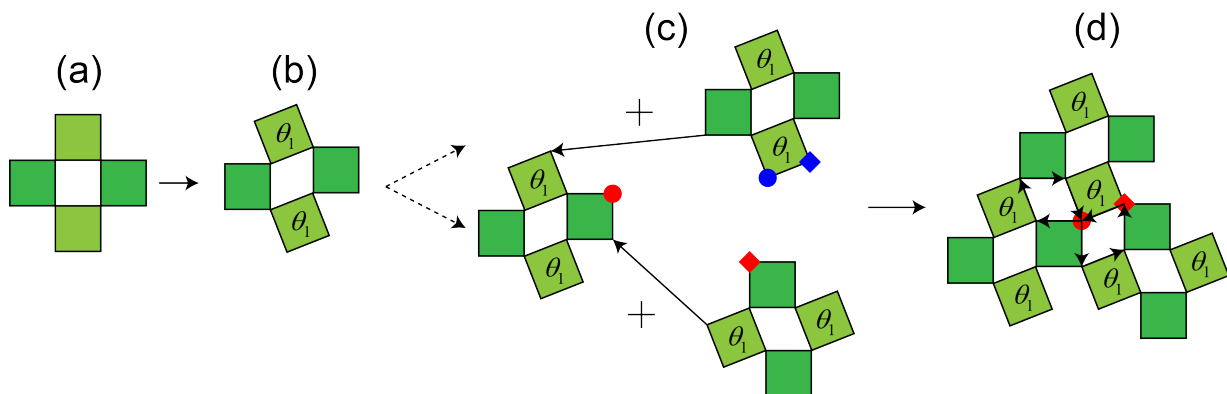


Figure S2: Geometrical compatibility of a unit cell with four squares. θ_1 indicates the rotation angle of the light-green squares. Geometrical compatibility between adjacent unit cells requires that the red and blue markers overlap in pairs (i.e. red round/diamond marker overlap with blue round/diamond markers).

Next, we focus on a unit cell consisting of four corner-connected squares with edge L_0 (see Fig. S2-a). First, we notice that compatibility within the unit cell requires that opposite squares undergo the same rotation. Therefore, without loss of generality, we assume that two of the four squares rotate by an angle θ_1 and two do not rotate (see Fig. S2-b). It is easy to see that in this case compatibility between adjacent unit cells is also satisfied (Fig. S2-c and d), indicating that the folding mechanism shown in Fig. S2-d is supported by the structure. Although, for the sake of brevity, here we do not include analysis for unit cells of larger size, these are straightforward. Such analysis indicate that this folding mechanism is the only one supported by the structure, resulting in a pattern of rhombic, elongated holes with the major axis perpendicular to each other (see Fig. S3).

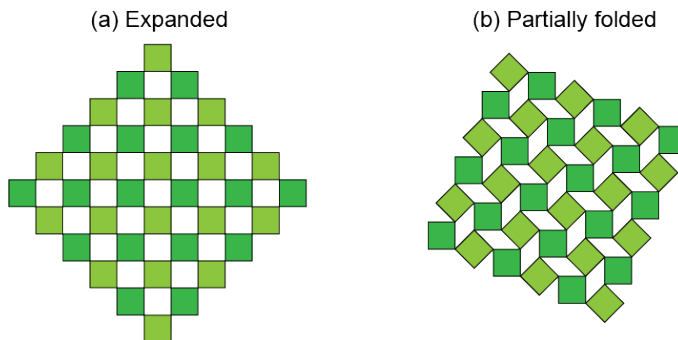


Figure S3: The folding mechanism for a network of rigid squares. (a) Expanded configuration. (b) Partially folded configuration.

Network of rigid triangles

We now proceed to investigate the folding mechanisms of a network of connected triangles arranged to form a kagome structure. First, we consider a unit cell consisting of only two triangles, which is the smallest unit cell for the network, and identify one folding mechanism for the system. Then, we focus on a larger unit cell comprising four triangles and find an additional folding mechanism. Finally, we establish a simple rule that enables us to easily construct the folding mechanisms for unit cells of arbitrary size.

Unit cell with two triangles

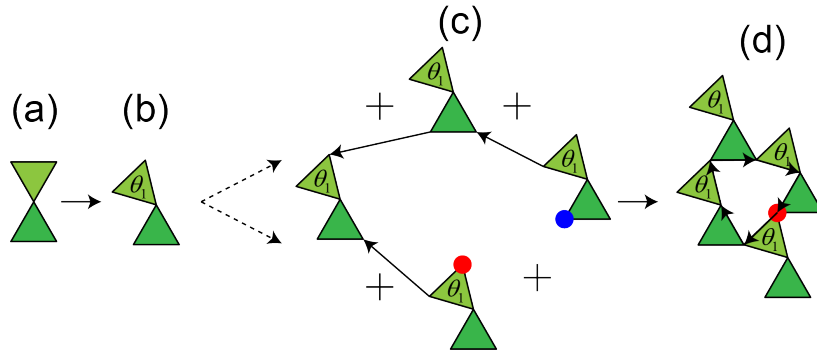


Figure S4: Geometrical compatibility of a unit cell with two triangles. θ_1 indicates the rotation angle of the light-green triangle. Geometrical compatibility between adjacent unit cells requires the red and blue markers overlap.

Here we consider a unit cell consisting of two corner-connected triangles with edge L_0 (see Fig. S4-a). If one of the two triangles rotates by an angle θ_1 (see Fig. S4-b), geometrical compatibility requires that the red and blue circular markers in Fig. S4-c overlap, yielding

$$L_0 \cos\left(\frac{2\pi}{3}\right) + L_0 \cos\left(\frac{\pi}{3} + \theta_1\right) + L_0 \cos(0) + L_0 \cos\left(-\frac{\pi}{3} + \theta_1\right) + L_0 \cos\left(-\frac{2\pi}{3}\right) + L_0 \cos(-\pi + \theta_1) = 0, \quad (\text{S2})$$

$$L_0 \sin\left(\frac{2\pi}{3}\right) + L_0 \sin\left(\frac{\pi}{3} + \theta_1\right) + L_0 \sin(0) + L_0 \sin\left(-\frac{\pi}{3} + \theta_1\right) + L_0 \sin\left(-\frac{2\pi}{3}\right) + L_0 \sin(-\pi + \theta_1) = 0.$$

It is easy to see that Eqs. (S2) are automatically satisfied for any choice of $0 < \theta_1 < 2\pi/3$, indicating that the folding mechanism shown in Fig. S4-d is supported by the structure. Such folding mechanism results in the formation of a pattern where all hexagonal holes progressively reduce to 3 point star-like shapes (see Fig. S5).

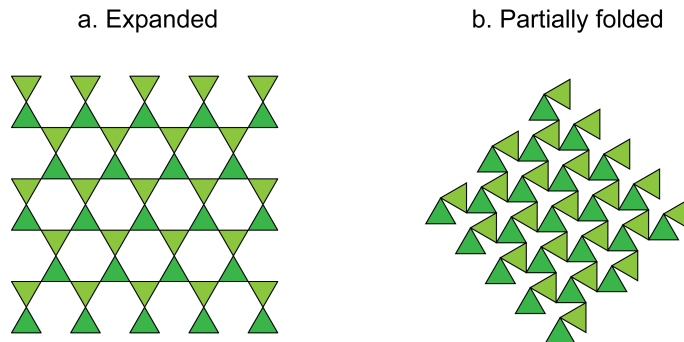


Figure S5: The folding mechanism of network of rigid triangles with a unit cell with two triangles. (a) Expanded configuration. (b) Partially folded configuration.

Unit cell with four triangles

Next, we focus on a unit cell comprising of four corner-connected triangles, as shown in Fig. S6-a. Without loss of generality we assume that one triangle does not rotate, while the other three triangles rotate by angles θ_1 , θ_2 and θ_3 (Fig. S6-b). Geometrical compatibility between adjacent unit cells requires

$$L_0 \cos\left(\frac{2\pi}{3}\right) + L_0 \cos\left(\frac{\pi}{3} + \theta_1\right) + L_0 \cos(\theta_2) + L_0 \cos\left(-\frac{\pi}{3} + \theta_1\right) + L_0 \cos\left(-\frac{2\pi}{3}\right) + L_0 \cos(-\pi + \theta_3) = 0, \quad (\text{S3})$$

$$L_0 \sin\left(\frac{2\pi}{3}\right) + L_0 \sin\left(\frac{\pi}{3} + \theta_1\right) + L_0 \sin(\theta_2) + L_0 \sin\left(-\frac{\pi}{3} + \theta_1\right) + L_0 \sin\left(-\frac{2\pi}{3}\right) + L_0 \sin(-\pi + \theta_3) = 0,$$

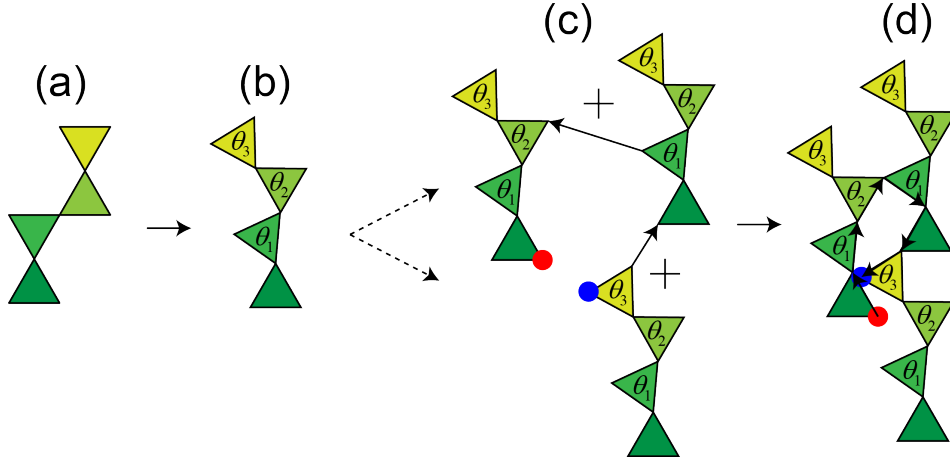


Figure S6: Geometrical compatibility of a unit cell with four triangles. θ_1 , θ_2 , and θ_3 indicates the rotation of the green, light-green and yellow triangles, respectively. Geometrical constraints between adjacent unit cells require the red and blue markers overlap.

which can be easily simplified to

$$-1 + \cos(\theta_1) + \cos(\theta_2) - \cos(\theta_3) = 0, \quad (\text{S4})$$

$$\sin(\theta_1) + \sin(\theta_2) - \sin(\theta_3) = 0.$$

Eqs. (S4) are automatically satisfied for

$$\begin{cases} \theta_1 = \theta_3, \\ \theta_2 = 0, \end{cases} \quad (\text{S5})$$

and

$$\begin{cases} \theta_1 = 0, \\ \theta_2 = \theta_3. \end{cases} \quad (\text{S6})$$

The first solution (Eqs. (S5)) results in the formation of the same pattern found when investigating the unit cell consisting of two triangles, as shown in Fig. S5. The second solution (Eqs. (S6)) is associated to the formation of a pattern of sheared voids where the shear direction alternates back and forth from row to row (see Fig. S7).

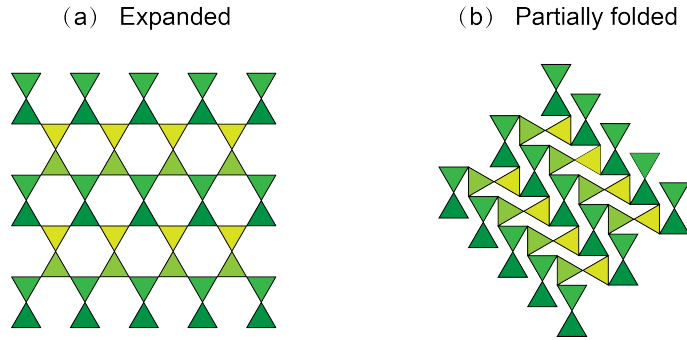


Figure S7: The additional folding mechanism of network of rigid triangles with a unit cell of four triangles. (a) Expanded configuration. (b) Partially folded configuration.

Folding mechanisms for larger unit cells

Additional folding mechanisms for the kagome network can be identified by repeating similar calculations as reported above for larger unit cells. Furthermore, the construction of additional folding mechanisms is greatly facilitated by

the observation that geometric compatibility requires the triangles to rotate by $\pm\alpha$ (i.e. by the same amount either in clockwise or anti-clockwise direction, see magenta and cyan triangles in Fig. S8) or not to rotate at all (i.e. $\alpha = 0$, see yellow triangles in Fig. S8). Although here, for the sake of brevity, we do not report the calculations to identify the folding mechanisms for larger unit cells, in Fig. S8 we show several of them.

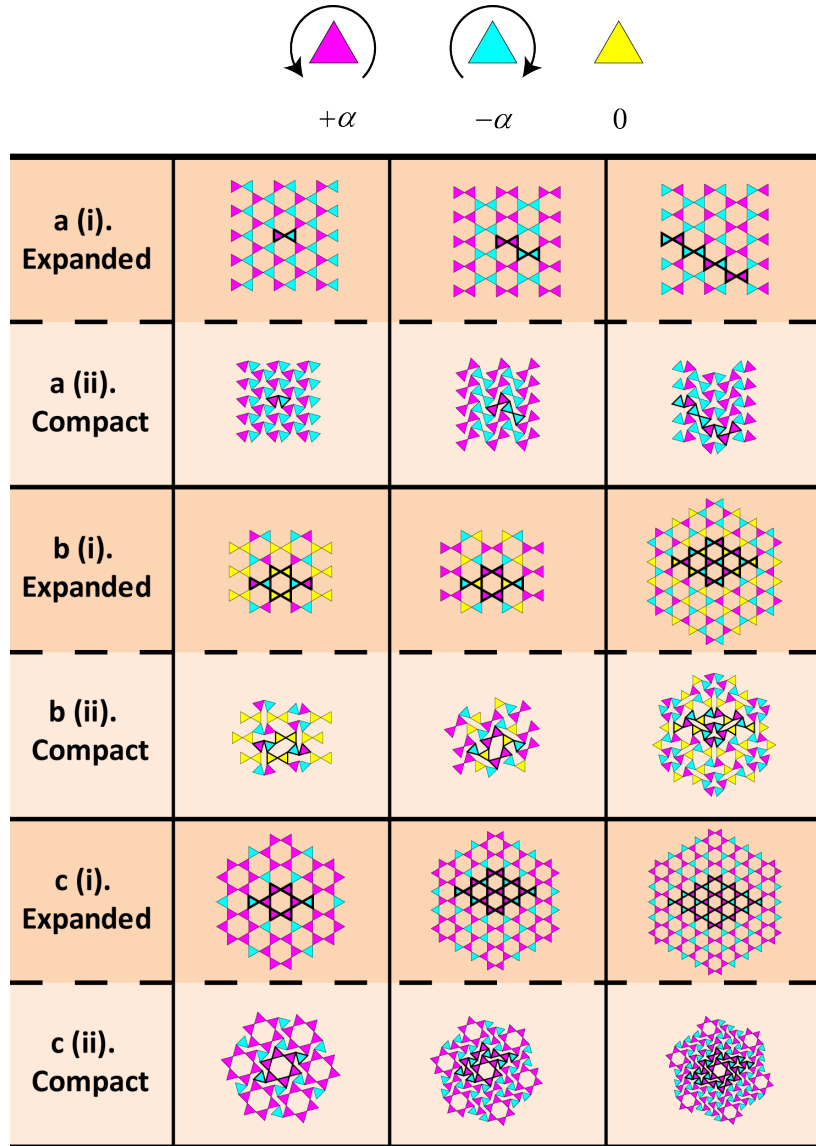


Figure S8: Nine folding mechanisms for a triangular network of connected triangles. The unit cell for each folding mechanism is outlined in black.

FINITE ELEMENT SIMULATIONS

Stability analysis: chiral pattern as linear combination of the X- and Z-mode

As shown in Fig. 3 of the main text our stability analysis reveals that for all considered values of θ (i.e. $\pi < \theta < 3\pi/2$), the X- and Z-modes are always triggered either as first or second mode. In particular, for $\pi < \theta < 5\pi/4$ the critical loading parameter λ_{cr} associated to the X-mode is found to be always lower than that associated to the Z-mode, so that the X-mode is expected to emerge during deformation for this range of loading path angles. By contrast, the Z-mode is expected to be triggered when $5\pi/4 < \theta < 3\pi/2$, since in this case the lowest critical loading

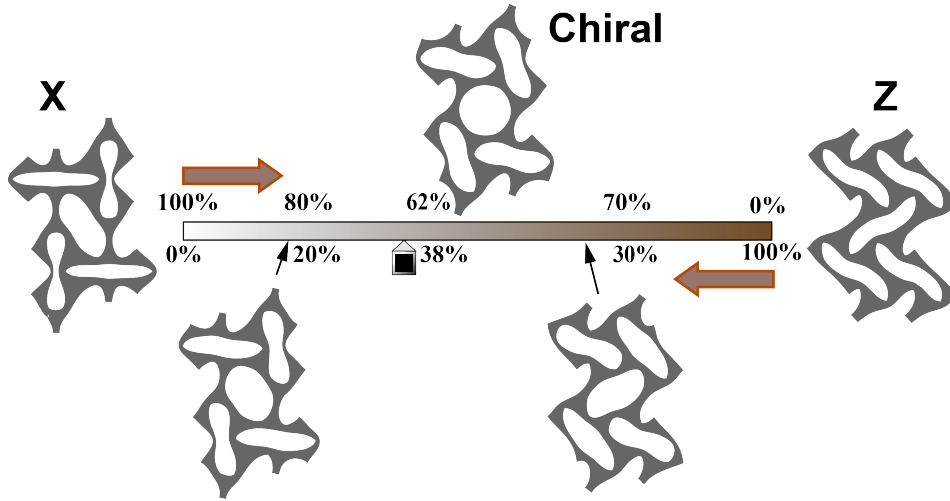


Figure S9: Schematic illustration of superimposition of X- and Z-modes. The chiral mode appears by a linear combination of the X- and Z- modes.

parameter is that corresponding to the Z-mode. Interestingly, for $\theta = 5\pi/4$ both the X- and Z-modes are characterized by the same critical loading parameter, so that any linear combination of the two modes is a valid eigenmode.

In Fig. S9 we report both the X- and Z-modes and three linear combinations of them. Interestingly, one of these linear combinations corresponds to a chiral pattern comprising six highly deformed voids surrounding an undeformed one, resembling that reported in Fig. 1-e of the main text for the kagome network.

Next, guided by the stability analysis we conduct a post-buckling analysis on a RVE consisting of 2×2 unit cells by applying periodic boundary conditions and introducing a geometrical imperfection with the form of the first two eigenmodes (i.e. a linear combination of the X- and Z- modes). As shown in Fig. 4-c of the main text, for $\theta = 5\pi/4$ a chiral pattern resembling that reported in Fig. S9 emerges.

Elastic wave propagation analysis

In order to obtain the dispersion relation for a triangular array of circular holes in an elastomeric matrix and to investigate the effect of the applied deformation on the propagation of elastic waves, frequency domain wave propagation analyses are performed on both the undeformed and deformed configurations generated by the post-buckling analysis using the finite element method [2, 3]. To work with the complex-valued displacements of the Bloch-wave calculation within the confines of a commercial code, all fields are split into real and imaginary parts [2]. In this way the equilibrium equations split into two sets of uncoupled equations for the real and imaginary parts. Thus, the eigenfrequency ω can be computed for any wave vector \mathbf{k} using two identical finite-element meshes for the RVE, one for the real part and the other for the imaginary part, and coupling them by Bloch-type displacement boundary conditions.

The phononic bandgaps are identified by checking all eigenfrequency $\omega(\mathbf{k})$ for all \mathbf{k} vectors in the irreducible Brillouin zone. The bandgaps (i.e. range in frequencies for which the propagation of waves is barred) are given by the frequency ranges within which no $\omega(\mathbf{k})$ exists. Numerically, a discrete set of \mathbf{k} vectors in the irreducible Brillouin zone need to be chosen in the analysis. For the simulations presented in this paper, five-segment wave-vector paths $\mathbf{G} - \mathbf{X} - \mathbf{M} - \mathbf{G} - \mathbf{Y} - \mathbf{M}$ defining the perimeter and the diagonal of the irreducible Brillouin zone are considered and the eigenfrequencies $\omega(\mathbf{k})$ are calculated for twenty points uniformly distributed on each line segment.

Note that all the calculations are performed on an enlarged unit cell (comprising 2×2 unit cells) with size dictated by the new periodicity introduced by buckling, as shown in Fig. S10-a. Such RVE is spanned by the lattice vectors $\mathbf{a}_1 = [a, 0]$ and $\mathbf{a}_2 = [0, \sqrt{3}a]$, where a is the center-to-center distance between adjacent holes and can be expressed as a function of the porosity ψ_o and hole diameter D_0 as $a = \left(\frac{\sqrt{3}\pi D_0^2}{6\psi_o}\right)^{1/2}$. Therefore the reciprocal space is defined by,

$$\mathbf{b}_1 = 2\pi \frac{\mathbf{a}_2 \times \mathbf{z}}{\|\mathbf{z}\|^2}, \quad \mathbf{b}_2 = 2\pi \frac{\mathbf{z} \times \mathbf{a}_1}{\|\mathbf{z}\|^2}, \quad (\text{S7})$$

where $\mathbf{z} = \mathbf{a}_1 \times \mathbf{a}_2$.

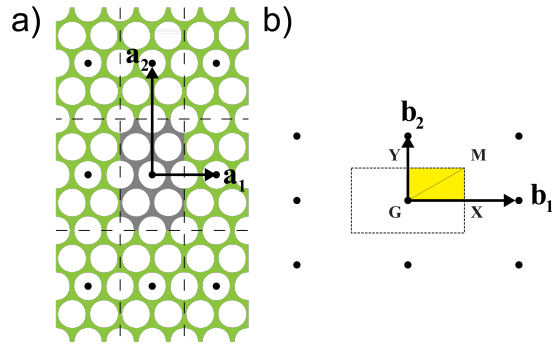


Figure S10: (a) Schematic of the structure in the undeformed configuration. The considered RVE spanned by the lattice vectors \mathbf{a}_1 and \mathbf{a}_2 is shown in grey. (b) The corresponding Brillouin zone in reciprocal space is spanned by the vectors \mathbf{b}_1 and \mathbf{b}_2 .

EXPERIMENTS

Biaxial compression tests

To verify findings from numerical models that show multiple folding mechanisms depending on the loading directions, we did experiments using a custom set-up that can control the loading in two orthogonal directions independently providing the capability to test the sample in arbitrary biaxial loading conditions. (see Fig. S11-a)

Biaxial compression tests were conducted on two perpendicularly placed linear quasi-static stages (model SLP-35 from Nippon Pulse America Inc.) in a displacement-controlled manner. The stages were configured to realize an optimal spatial resolution of $1 \mu\text{m}$. The fine movement of the stages was coordinated through a LabView program and the ratio between the engineering strains in two directions was kept constant during the biaxial test. The specimens were compressed through a set of customary compression fixtures, which were designed to ensure them not to collide during the compression tests (see Fig. S11-b). The overall fixture set consisted of two pairs of parts with each pair for the compressive movement in one of two orthogonal directions. The specimen was not clamped to the fixtures because the friction between the specimen and fixture surface was enough to hold the specimen. Lubricant was used on surfaces of fixtures to reduce friction and boundary effects. The compression tests were performed at the cross-head velocity of $5\text{mm}/\text{min}$ until the structure was densified. During the test, a Nikon D90 SLR camera was used to capture the resulting patterns from the sample.

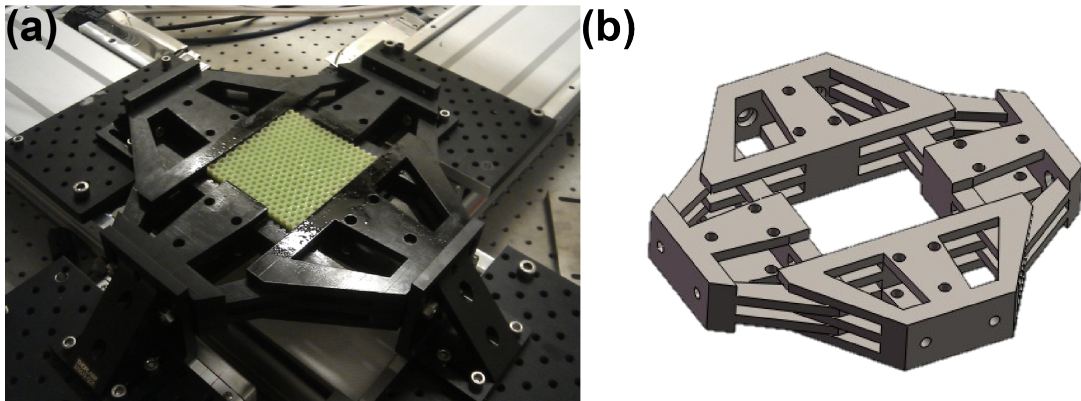


Figure S11: (a) Picture of the biaxial setup used for our compression test. (b) Sketch of the biaxial compression fixture whused for our compression experiments.

Wave propagation tests

To investigate the effect of different instability-induced patterns on the propagation of small amplitude elastic waves in the periodic structure, we conducted wave propagation tests for the the udeformed sample and for three deformed

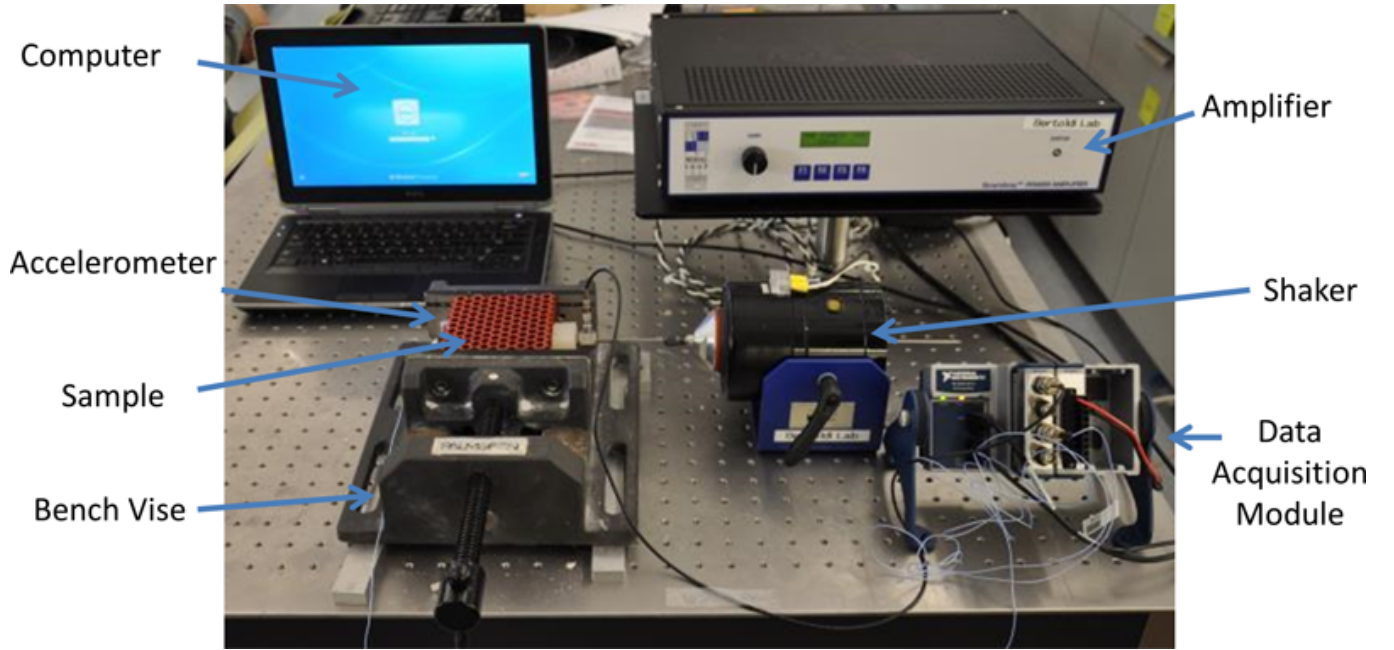


Figure S12: Picture of the set-up used for our wave propagation tests.

configurations obtained by different loading path angles $\theta = \pi, 5\pi/4$ and $3\pi/2$, but under the same areal strain, $\epsilon_{Area} = -0.24$.

The overall set-up for the tests is shown in Fig. S12. All components were placed on top of a passive optical table (model PTM11104 from Thorlabs) to isolate from ambient vibrations. First, a Gaussian white noise was generated from the amplifier and was used to control the shaker (model K2025E013 from The Modal Shop). The dynamic response was recorded using a miniature accelerometer (352C22 PCB Piezotronics) attached to the far end of the sample. To apply a uniform in-plane wave, we used a PTFE (Polytetrafluoroethylene) block to increase the contact area between the shaker and the sample. Furthermore, to effectively transmit the vibration from the shaker to the sample, all contact interfaces (shaker/PTFE block, PTFE block/sample, sample/accelerometer) were temporarily super-glued.

The input force signals were detected at the shaker (input) from a load cell. The acceleration at the far end of the sample (output) was detected using an ultra-light piezo-electric accelerometer. The detected signal was acquired through a data acquisition module and further processed and recorded by a computer. The transmittance was computed as the ratio between the output acceleration signal recorded at the far end of the sample and the input force signal from the load cell (i.e., $\|A(\omega)/F(\omega)\|$).

A bench vise was used to apply the desired value of deformation to the sample (see Fig. S13). In Fig. S13-b and -c we show the sample deformed into the in X-mode and Z-mode, respectively. In these cases, the shaker was directly connected to one end of the sample. Differently, when the system was deformed equibiaxially, four clamps are needed, so that all four edges of the sample were in contact with the fixture (see Fig. S13-d). In this case the input wave from the shaker was transmitted through an inserted long rod and the output wave was detected from another inserted long rod away from the input.

-
- [1] V. Kapko, M. Treacy, M. Thorpe, and S. Guest, Proc. R. Soc. A **465**, 3517 (2009).
 - [2] K. Bertoldi and M. C. Boyce, Phys. Rev. B **78**, 184107 (2008).
 - [3] P. Wang, J. Shim, and K. Bertoldi, Phys. Rev. B **88**, 014304 (2013).

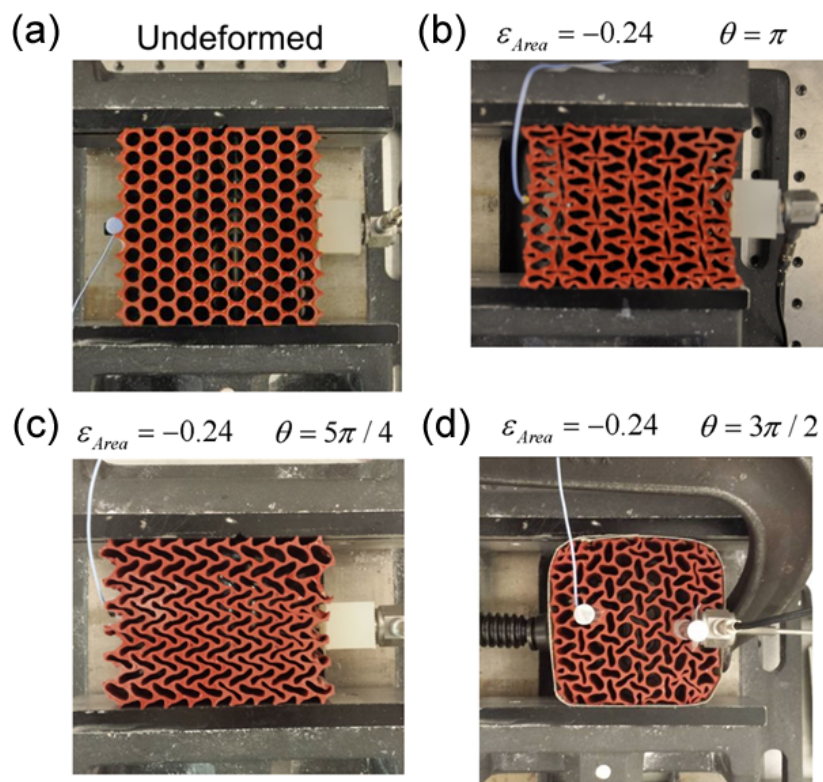


Figure S13: (a) Picture of the undeformed sample with the shaker and accelerometer connected to it. (b) Picture of the sample deformed into the X-mode with the shaker and accelerometer connected to it. (c) Picture of the sample deformed into the Z-mode with the shaker and accelerometer connected to it. (d) Picture of the sample deformed into the chiral mode with the shaker and accelerometer connected to it.